

1 Disproportionately strong climate forcing
2 from extratropical explosive volcanic
3 eruptions

4

5 Matthew Toohey^{*,1}, Kirstin Krüger², Hauke Schmidt³, Claudia Timmreck³, Michael Sigl^{2,4,5},

6 Markus Stoffel^{6,7,8}, Rob Wilson^{9,10}

7 ¹GEOMAR Helmholtz Centre for Ocean Research Kiel, Germany

8 ²University of Oslo, Department of Geosciences, Oslo, Norway

9 ³Max Planck Institute for Meteorology, Hamburg, Germany

10 ⁴Laboratory of Environmental Chemistry, Paul Scherrer Institute, 5232 Villigen, Switzerland

11 ⁵Oeschger Centre for Climate Change Research, 3012 Bern, Switzerland

12 ⁶Climate Change Impacts and Risks in the Anthropocene (C-CIA), Institute for Environmental
13 Sciences, University of Geneva, Boulevard Carl-Vogt 66, CH-1205 Geneva, Switzerland

14 ⁷dendrolab.ch, Department of Earth Sciences, University of Geneva, Rue des Maraîchers 13, CH-
15 1205 Geneva, Switzerland

16 ⁸Department F.-A. Forel for Aquatic and Environmental Sciences, University of Geneva,
17 Boulevard Carl-Vogt 66, CH-1205 Geneva, Switzerland

18 ⁹School of Earth and Environmental Sciences, University of St Andrews, Fife KY16 9AL, UK

19 ¹⁰Lamont-Doherty Earth Observatory, Columbia University, Palisades NY 10964, USA

20 *Corresponding author

21

22 **Abstract**

23 Extratropical volcanic eruptions are commonly thought to be less effective at driving large-scale
24 surface cooling than tropical eruptions. However, recent minor extratropical eruptions have
25 produced a measurable climate impact, and proxy records suggest that the most extreme
26 Northern Hemisphere cold period of the Common Era was initiated by an extratropical eruption
27 in 536 CE. Using ice core-derived volcanic stratospheric sulfur injections and Northern
28 Hemisphere summer temperature reconstructions from tree rings, we show here that in
29 proportion to their estimated stratospheric sulfur injection, extratropical explosive eruptions
30 since 750 CE have produced stronger hemispheric cooling than tropical eruptions. Stratospheric
31 aerosol simulations demonstrate that for eruptions with sulfur injection magnitude and height
32 equal to that of the 1991 Mt. Pinatubo eruption, extratropical eruptions produce time-
33 integrated radiative forcing anomalies over the Northern Hemisphere extratropics up to 80%
34 greater than tropical eruptions, as decreases in aerosol lifetime are overwhelmed by the
35 enhanced radiative impact associated with the relative confinement of aerosol to a single
36 hemisphere. The model results are consistent with the temperature reconstructions, and
37 elucidate how the radiative forcing produced by extratropical eruptions is strongly dependent
38 on eruption season and sulfur injection height within the stratosphere.

39 **Main**

40 Major volcanic eruptions impact climate through the injection of sulfur into the stratosphere,
41 leading to the production of stratospheric sulfate aerosol, which scatters incoming solar
42 radiation and cools the Earth's surface¹. The climatic impact of any eruption depends on the
43 properties of the stratospheric aerosol enhancement, and is tied principally to the amount of
44 sulfur injected, but also to the aerosol's atmospheric lifetime, spatial spread, and size
45 distribution.

46 It is commonly thought that extratropical eruptions have a weaker climatic impact than tropical
47 eruptions^{2,3}. This hypothesis rests on the idea that aerosol resulting from tropical eruptions
48 spreads globally, and has a longer stratospheric lifetime due to a longer transport path from the
49 tropics to removal across the mid- or high-latitude tropopause⁴. Shorter lifetimes for
50 stratospheric aerosol from extratropical eruptions have been assumed in prior volcanic forcing
51 reconstructions^{5,6} and are thus implicit in model studies which support the idea of weaker
52 climate forcing from extratropical eruptions⁴.

53 Comparing the aerosol clouds and climate impacts resulting from tropical vs. extratropical
54 eruptions based on observations and proxy records is complicated by a number of confounding
55 factors. During the satellite era, stratospheric sulfur injections from the strongest extratropical
56 eruptions have been an order of magnitude weaker than the largest tropical eruptions⁷. On
57 longer timescales, ice cores record sulfate from major eruptions from both the tropics and
58 extratropics⁸, however, limited knowledge of the height of the volcanic sulfur injection from
59 those eruptions adds uncertainty to estimates of radiative forcing from ice cores⁹.

60 Interest in extratropical eruptions has recently increased, due in part to a series of minor
61 extratropical volcanic eruptions which produced significant radiative forcing on climate,
62 counteracting a portion of greenhouse gas warming^{10,11}. Furthermore, model results suggest
63 the hemispherically asymmetric radiative forcing from extratropical eruptions has distinct
64 impacts on tropical precipitation^{12,13}, and atmospheric and ocean circulation^{14,15}.
65 Reconstructions of volcanic activity spanning the past 2500 years from ice cores have identified
66 large extratropical volcanic events with associated large-scale cooling⁸, including extreme NH
67 cold conditions initiated by an extratropical eruption around the year 536 CE^{8,16,17}. These
68 findings motivate a re-examination of the radiative forcing and climate impacts of extratropical
69 eruptions.

70 **Hemispheric cooling by extratropical vs. tropical eruptions**

71 Reconstructions of Northern Hemisphere (NH) extratropical summer temperatures over land
72 from tree rings show a clear cooling response to volcanic eruptions¹⁸. Here, we examine the
73 magnitude of the cooling recorded in three tree ring NH temperature reconstructions^{19–21} over
74 the 750–2000 CE period, supplemented with estimates of eruption region and volcanic
75 stratospheric sulfate injection (VSSI) deduced from ice core sulfate records²². We select
76 eruptions with VSSI > 2 Tg S, excluding cases potentially affected by prior eruptions (see
77 Methods, Supplementary Table 1) and five events linked to Iceland (Supplementary Table 2).
78 Post-volcanic 3-year mean NH temperature anomalies, averaged over the three reconstructions
79 (ΔT_{3yr}^{ALL} , see Methods) show a clear relationship with VSSI (Fig. 1). Tropical eruptions show a
80 particularly coherent correlation ($r = -0.68$) between temperature and VSSI. There is also clearly

81 scatter in the relationship between $\Delta T_{3\text{yr}}$ and VSSI, which can be due to uncertainties in both
82 quantities, but also the influences of internal climate variability on $\Delta T_{3\text{yr}}$ and the impact of
83 secondary eruption characteristics such as eruption season and plume height. Ratios of
84 temperature response to VSSI (Supplementary Tables 4 and 5, Fig. 1 inset) show a broad range
85 of values, with outliers including events with apparent post-eruption warming to very strong
86 apparent cooling. On average, tropical and extratropical eruptions lead to ΔT -to-VSSI ratios of -
87 $0.025 \pm 0.005 \text{ }^\circ\text{C (Tg S)}^{-1}$ and $-0.080 \pm 0.018 \text{ }^\circ\text{C (Tg S)}^{-1}$ respectively (Table 1). The difference
88 between the ΔT -to-VSSI ratios for extratropical and tropical eruptions is significant at the 99%
89 level ($p=0.006$): a factor of roughly 2-4 difference is consistent across the three NH temperature
90 reconstructions (Table 1, Supplementary Fig. 1).

91 The stronger temperature response per unit VSSI to extratropical eruptions is based on a
92 sample of extratropical eruptions with VSSI mostly limited to values less than 7 Tg S
93 (Supplementary Table 4). While this limits the comparability of the temperature responses to
94 extratropical and tropical eruptions, we note that the mean ΔT -to-VSSI ratios for tropical
95 eruptions are consistent between eruptions less than and greater than 7 Tg S (Fig. 1 inset),
96 suggesting that the stronger ΔT -to-VSSI ratios seen for extratropical eruptions are likely
97 representative. The ΔT -to-VSSI ratio for extratropical eruptions after 750 CE is consistent with
98 the strong cooling estimated for the 536 CE eruption, albeit from a single reconstruction (Fig. 1,
99 Supplementary Table 5). On the other hand, the extratropical eruptions of 626 and 1180 CE
100 produce ΔT -to-VSSI ratios on par with tropical eruptions.

101 One pertinent issue in the calculation of ΔT -to-VSSI ratios is uncertainty in the methods used to
102 calculate VSSI, which apply a smaller transfer function for extratropical eruptions than tropical
103 eruptions in the estimation of volcanic aerosol from ice core sulfate^{22,23}. Nonetheless, if VSSI
104 values for extratropical eruptions were calculated as for tropical eruptions, extratropical
105 eruptions would still produce an 81% stronger average ΔT -to-VSSI ratio than tropical eruptions
106 (Table 1).

107 Since aerosol from extratropical eruptions is largely contained within the hemisphere of the
108 eruption²⁴, while that from tropical eruptions spreads globally, a factor of two difference
109 between ΔT -to-VSSI ratios for extratropical and tropical eruptions could be explained by a
110 relatively equal temperature response to hemispheric aerosol loading, irrespective of latitude
111 of injection. This explanation however seemingly contradicts the expectation of a significantly
112 reduced stratospheric aerosol lifetime for extratropical eruptions.

113 **The lifetime of volcanic stratospheric sulfur**

114 To investigate the impact of eruption latitude on the volcanic stratospheric sulfate aerosol
115 evolution we performed ensemble simulations with the coupled aerosol-atmospheric general
116 circulation model MAECHAM5-HAM (see Methods). All simulations include a stratospheric
117 injection of 8.5 Tg S, consistent with satellite-based estimates of the 1991 Pinatubo eruption²⁵,
118 with eruptions in both January and July to include the effect of season^{20,26,27}. A set of four
119 eruption latitudes were chosen based on maxima in the latitudinal distribution of identified
120 eruptions within the Volcanoes of the World database²⁸ (Supplementary Fig. 2), and simulations
121 (Supplementary Table 6) were performed with SO₂ injected at each latitude and 30 hPa (~24
122 km), consistent with the 1991 Pinatubo eruption. Eruptions at 56°N were also performed with

123 injections into the lower stratosphere at 100 hPa (~16 km) and 150 hPa (~13 km), roughly
124 consistent with the range of estimates⁷ of the injection heights of recent minor (VSSI < 1 Tg S)
125 extratropical eruptions including Kasatochi (2008, 52°N) and Sarychev (2009, 48°N).

126 The simulated spatiotemporal evolution of volcanic aerosol burden (Fig. 2a-d, Supplementary
127 Fig. 3) shows global spread of aerosol following tropical eruptions and hemispheric
128 containment of aerosol for extratropical eruptions. These patterns of aerosol spread are
129 consistent with prior simulations²⁴, comparisons of tropical vs. extratropical temperature
130 reconstructions²⁹ and understanding of the general features of large-scale circulation within the
131 stratosphere³⁰.

132 For sulfur injections at a fixed height of 30 hPa, global mean sulfate mass burdens show
133 sensitivity to both the injection latitude and season (Fig. 2e, f). For January (i.e., NH winter)
134 eruptions, extratropical eruptions produce sulfate burdens which are similar to tropical
135 eruptions, with stratospheric e-folding lifetimes only ~10% smaller (Fig. 2g). For July (i.e., NH
136 summer) eruptions, global sulfate burdens from extratropical eruptions reach maxima similar
137 to those from tropical eruptions, but decay faster, with lifetimes 24-44% shorter.

138 Simulations of sulfur injections at 56°N with varying injection heights show that injection height
139 within the stratosphere plays an important role in controlling the lifetime of stratospheric
140 sulfate. The lifetimes of stratospheric sulfur for extratropical injections at 100 hPa and 150 hPa
141 are notably shorter than from both tropical and extratropical 30 hPa injections (Fig. 2g). These
142 results can be understood as arising from differences in transport processes between the
143 lowermost stratosphere (LMS) and “overworld”³¹. In the LMS, defined as the region between

144 the tropopause and the 380 K potential temperature surface, large-scale two-way transport
145 along potential temperature isentropes exchanges air between the tropopause and
146 stratosphere, while in the overworld, isentropes do not cross the tropopause and therefore
147 transport simply redistributes mass within the stratosphere. Sulfate aerosol resulting from
148 simulated sulfur injection into the LMS are transported into the troposphere and deposited to
149 the surface rapidly after the injection (Supplementary Fig. 4), whereas cross-tropopause
150 transport of sulfur injected into the extratropical stratospheric overworld only proceeds after
151 aerosol has descended into the LMS, which prolongs the aerosol lifetime.

152 **Global mean aerosol properties and radiative forcing**

153 The radiative impact of stratospheric aerosol depends not only on its mass, but also on its size
154 distribution³², since stratospheric sulfate aerosol has maximum scattering efficiency at effective
155 radius of $\sim 0.2 \mu\text{m}$, with decreasing efficiency for the larger effective radii observed after major
156 eruptions^{33,34}. Sulfate-mass-weighted mean effective radius ($\langle r_{\text{eff}} \rangle$, see Methods) and global
157 mean stratospheric aerosol optical depth (SAOD) are shown in Fig. 3 as a function of injection
158 location. Simulated effective radius shows sensitivity to eruption latitude, season and injection
159 height (Fig. 3a, b). For January 30 hPa injections, the evolution of $\langle r_{\text{eff}} \rangle$ is similar for
160 extratropical and tropical eruptions, with a peak $\langle r_{\text{eff}} \rangle$ of around $0.4 \mu\text{m}$. For July 30 hPa
161 injections, simulated $\langle r_{\text{eff}} \rangle$ for extratropical eruptions reaches much larger values ($>0.6 \mu\text{m}$)
162 than comparable tropical eruptions ($\sim 0.4 \mu\text{m}$). Sulfur injections into the extratropical lower
163 stratosphere (100 and 150 hPa) result in lower $\langle r_{\text{eff}} \rangle$ compared to 30 hPa injections, with again,
164 July eruptions leading to larger $\langle r_{\text{eff}} \rangle$ than January eruptions. The sensitivity of $\langle r_{\text{eff}} \rangle$ to eruption
165 latitude, season and injection height can be understood to be primarily controlled by the

166 availability of hydroxyl radical (OH), which controls the rate of SO₂-to-H₂SO₄ conversion. Higher
167 OH values, which occur in the high-latitude stratosphere during summer (Supplementary Fig. 5),
168 lead to faster H₂SO₄ production. When H₂SO₄ production is fast compared to stratospheric
169 mixing and transport processes, H₂SO₄ concentrations are relatively enhanced at a local to
170 regional scale, promoting aerosol growth through condensation and coagulation.

171 SAOD at 550 nm quantifies the attenuation of solar radiation by aerosol, and is a function of the
172 sulfate burden as well as effective radius. January extratropical 30 hPa injections lead to a
173 global mean SAOD (Fig. 3c) very similar to tropical 30 hPa eruptions, reflecting similar global
174 sulfate burdens and $\langle r_{\text{eff}} \rangle$. July extratropical 30 hPa injections lead to a much weaker global
175 mean SAOD than tropical 30 hPa eruptions (Fig. 3d), due to both the faster decay of the sulfate
176 burden and larger $\langle r_{\text{eff}} \rangle$. In terms of three-year cumulative SAOD (Fig 3e), extratropical 30 hPa
177 injections in January produce only ~10% less global mean SAOD than comparable tropical
178 eruptions, while extratropical 30 hPa eruptions in July produce 30% (36°N) to 53% (56°N) less
179 SAOD compared to tropical counterparts. Injections into the extratropical lower stratosphere in
180 general lead to smaller SAOD than injections to 30 hPa, although due to the smaller $\langle r_{\text{eff}} \rangle$ for
181 lower injection heights, the impact of injection height is weaker on SAOD than on sulfate
182 burden lifetime. The importance of r_{eff} is especially apparent for July eruptions at 56°N, where
183 the simulated peak and cumulative SAOD resulting from an 100 hPa injection is similar to that
184 from a 30 hPa injection, despite a smaller sulfate burden.

185 Post-volcanic surface temperature anomalies result from the impact of aerosol on atmospheric
186 radiative transfer, which is often quantified as radiative forcing (W m⁻²). The radiative impact of

187 the simulated eruptions is quantified through the top-of-atmosphere net radiative anomalies:
188 since the simulations are performed with fixed sea surface temperatures (SST) and sea ice, this
189 is equivalent to the “fixed SST” version of effective radiative forcing (ERF)^{35,36}. Simulated global
190 mean ERF anomalies for extratropical eruptions (Supplementary Fig. 6) at 30 hPa are smaller
191 than that of corresponding tropical eruptions in the ensemble mean, although this difference is
192 as small as 15%, and in many cases the ensemble range for extratropical eruptions overlaps
193 with that of tropical eruptions. Global mean ERF anomalies for extratropical LMS injections
194 range from 57-91% smaller than for tropical eruptions.

195 **Impact of volcanic radiative forcing in the NH extratropics**

196 Modelling studies suggest that regional surface temperature responses to external radiative
197 forcing depend on the structure of the forcing, and that NH extratropical temperatures respond
198 predominantly to extratropical forcing³⁷. Since the NH tree ring-based temperature
199 reconstructions explored above are based on samples collected in the mid-to high latitudes, we
200 examine the simulated radiative forcing in the NH extratropics (NHext = 30-90°N).

201 Aerosol from extratropical eruptions is heavily concentrated within the NH (Fig. 2), and
202 particularly within the NHext where SAOD resulting from extratropical 30 hPa eruptions peak at
203 values up to 2-3 times larger than those of tropical 30 hPa injections (Fig. 4a,b). As a result,
204 NHext-averaged ERF (Fig 4c,d) from extratropical 30 hPa injections is stronger than that from
205 tropical 30 hPa injections. Three-year cumulative NHext-averaged ERF (Fig 4e) from
206 extratropical 30 hPa January injections are 70-80% stronger than the average of tropical 30 hPa
207 injections. Extratropical 30 hPa July injections, in contrast, produce cumulative NHext-averaged
208 ERF of -3 to +34% compared to tropical eruptions, indicating a strong sensitivity to eruption

209 season. Differences between tropical and extratropical injections are also apparent in the time
210 evolution of ERF: for January eruptions (Fig. 4c), peak ERF values for tropical 30 hPa and
211 extratropical lower stratosphere injections occur within the first four months, while ERF for
212 extratropical 30 hPa injections peaks 6 months after the eruption during NH summer. For July
213 eruptions (Fig. 4b), the peak forcing from extratropical injections occurs within the summer of
214 eruption, while that of tropical 30 hPa injections occurs 6-9 months later, during NH winter and
215 spring.

216 Results described above challenge the perception that extratropical eruptions are less
217 climatically important than tropical eruptions. While simulated SAOD and ERF are weaker for
218 NH extratropical eruptions than for tropical eruptions in the global mean, the hemispheric
219 confinement of aerosol results in stronger radiative anomalies over the NH, with NHex ERF for
220 extratropical eruptions up to 80% stronger than tropical eruptions. This result is consistent with
221 the stronger ΔT -to-VSSI ratio for extratropical eruptions in tree ring based NH temperature
222 reconstructions. While the tree rings imply a stronger difference between ΔT -to-VSSI ratios for
223 extratropical and tropical eruptions than model-based differences in radiative forcing, an 80%
224 stronger response to extratropical eruptions lies within the 2σ uncertainty range of the percent
225 differences in ΔT -to-VSSI ratio between extratropical and tropical eruptions. Furthermore,
226 quantitative differences between tree ring-based ΔT -to-VSSI ratios and model-based radiative
227 forcing may reflect non-linearity in temperature sensitivity to spatially inhomogeneous
228 radiative forcing³⁸, and uncertainties in proxy-based estimates. We note particularly that
229 quantitative agreement between ΔT -to-VSSI ratios and modeled radiative forcing is much

230 closer if VSSI values for extratropical eruptions were calculated using the same transfer function
231 as for tropical eruptions (Table 1).

232 **Implications for past and future extratropical eruptions**

233 Past reconstructions of volcanic forcing have assumed short stratospheric lifetimes and weak
234 radiative forcing of aerosol from extratropical eruptions. Our modeling experiments confirm a
235 shorter aerosol lifetime for extratropical injections, however, for a constant injection height in
236 the stratospheric overworld, the effect is as little as 10%. Our simulations demonstrate that the
237 lifetime of stratospheric aerosol from extratropical injections is strongly connected to the
238 injection height within the stratosphere. The assumption of a short lifetime for extratropical
239 eruptions in previous work⁴ is likely tied to an implicit assumption of lower injection heights.
240 However, volcanic plume models suggest that plume heights have weak dependence on
241 eruption latitude^{39,40}, and estimated maximum plume heights for the 1912 Katmai (58°N)
242 eruption based on estimated mass eruption rates and tephra dispersal reach 28 km⁴¹,
243 comparable to that of Pinatubo. Prior reconstructions of volcanic forcing, for example those^{5,42}
244 used in simulations of the Last Millennium as part of the fifth phase of the Coupled Model
245 Intercomparison Project⁴³, appear to underestimate the climate impact of extratropical
246 eruptions relative to tropical eruptions (Supplementary Fig. 7). More accurate reconstruction of
247 the magnitude and timing of past extratropical eruptions, and the optical properties of the
248 associated stratospheric aerosol, may increase the proportion of temperature variability
249 attributable to external forcing.

250 Strong sensitivity of simulated radiative forcing to the season and injection height of
251 extratropical eruptions—resulting from impacts on stratospheric lifetime, aerosol effective

252 radius and phasing between SAOD and incoming solar radiation²⁷—is consistent with the
253 scatter in the relationship between tree ring-derived cooling and VSSI for extratropical
254 eruptions. Reconstructions of volcanic forcing could therefore benefit from information of
255 season and injection height. Information on eruption season has been obtained in some cases
256 from high resolution analysis of ice cores⁴⁴, historical records^{20,45}, and geochemical analysis of
257 volcanic tephra in ice cores^{46–48}. Analysis of the isotopic composition of ice core sulfate has
258 been suggested as indicative of the height reached by the sulfate aerosol^{49–51}, although this
259 approach has been criticized on the basis that isotopic sulfur fractionation is related to the
260 height of aerosol with respect to the peak in the vertical profile of extratropical ozone
261 concentration rather than with respect to the tropopause⁹. Our model results suggest that
262 aerosol lifetime varies throughout the extratropical lower stratosphere, with an important
263 threshold being the interface between the LMS and overworld, which is comparable to the level
264 of peak ozone concentration. Thus, our results support the utility of sulfur isotope analysis for
265 providing valuable information on volcanic radiative forcing.

266 Volcanic eruptions with large VSSI have been less frequent in the extratropics than in the
267 tropics over recent centuries (Fig. 1). Many of the largest ice core sulfate signals from
268 extratropical eruptions originate from eruptions like Laki (1783/84 CE) that were at least partly
269 effusive⁵². In other cases, extratropical eruptions with large erupted mass like Changbaishan
270 (946 CE)⁵³ appear to have had a small VSSI. A clear example of an extratropical explosive
271 eruption with strong VSSI is that of the ca. 536 CE eruption, which produced solar dimming
272 lasting over a year⁵⁴, leading to some of the coldest NH temperatures of the Common Era. The
273 Common Era is however a short sample in geological terms, and the (admittedly incomplete⁵⁵)

274 Holocene volcanic record²⁸ suggests major (VEI \geq 5) eruptions are just as common in the NH
275 extratropics as in the tropics. Extratropical volcanic eruptions with large sulfur injections into
276 the stratospheric overworld have occurred in the past, and they will in the future. Our results
277 suggest that rather than reducing the radiative forcing and climate impact of such major
278 eruptions, the extratropical eruption latitude acts primarily to focus the radiative impacts
279 within the NH, strengthening its hemispheric climate impact.

280 **References**

- 281 1. Robock, A. Volcanic Eruptions and Climate. *Rev. Geophys.* **38**, 191–219 (2000).
- 282 2. Kirtman, B. *et al.* in *Climate Change 2013: The Physical Science Basis. Contribution of*
283 *Working Group I to the Fifth Assessment Report of the Intergovernmental Panel on*
284 *Climate Change* (eds. Stocker, T. F. *et al.*) 953–1028 (Cambridge University Press, 2013).
- 285 3. Myhre, G. *et al.* in *Climate Change 2013: The Physical Science Basis. Contribution of*
286 *Working Group I to the Fifth Assessment Report of the Intergovernmental Panel on*
287 *Climate Change* (eds. Stocker, T. F. *et al.*) 658–740 (Cambridge University Press, 2013).
- 288 4. Schneider, D. P., Ammann, C. M., Otto-Bliesner, B. L. & Kaufman, D. S. Climate response
289 to large, high-latitude and low-latitude volcanic eruptions in the Community Climate
290 System Model. *J. Geophys. Res.* **114**, D15101 (2009).
- 291 5. Gao, C., Robock, A. & Ammann, C. Volcanic forcing of climate over the past 1500 years:
292 An improved ice core-based index for climate models. *J. Geophys. Res.* **113**, D23111
293 (2008).
- 294 6. Ammann, C. M., Meehl, G. A., Washington, W. M. & Zender, C. S. A monthly and

- 295 latitudinally varying volcanic forcing dataset in simulations of 20th century climate.
296 *Geophys. Res. Lett.* **30**, 59–1 (2003).
- 297 7. Carn, S. A., Clarisse, L. & Prata, A. J. Multi-decadal satellite measurements of global
298 volcanic degassing. *J. Volcanol. Geotherm. Res.* **311**, 99–134 (2016).
- 299 8. Sigl, M. *et al.* Timing and climate forcing of volcanic eruptions for the past 2,500 years.
300 *Nature* **523**, 543–549 (2015).
- 301 9. Schmidt, A., Thordarson, T., Oman, L. D., Robock, A. & Self, S. Climatic impact of the long-
302 lasting 1783 Laki eruption: Inapplicability of mass-independent sulfur isotopic
303 composition measurements. *J. Geophys. Res.* **117**, D23116 (2012).
- 304 10. Santer, B. D. *et al.* Volcanic contribution to decadal changes in tropospheric temperature.
305 *Nat. Geosci.* **7**, 185–189 (2014).
- 306 11. Solomon, S. *et al.* The Persistently Variable ‘Background’ Stratospheric Aerosol Layer and
307 Global Climate Change. *Science* **333**, 866–70 (2011).
- 308 12. Haywood, J. M., Jones, A., Bellouin, N. & Stephenson, D. Asymmetric forcing from
309 stratospheric aerosols impacts Sahelian rainfall. *Nat. Clim. Chang.* **3**, 660–665 (2013).
- 310 13. Colose, C. M., LeGrande, A. N. & Vuille, M. The influence of volcanic eruptions on the
311 climate of tropical South America during the last millennium in an isotope-enabled
312 general circulation model. *Clim. Past* **12**, 961–979 (2016).
- 313 14. Pausata, F. S. R., Chafik, L., Caballero, R. & Battisti, D. S. Impacts of high-latitude volcanic
314 eruptions on ENSO and AMOC. *Proc. Natl. Acad. Sci.* **112**, 13784–13788 (2015).
- 315 15. Stevenson, S., Fasullo, J. T., Otto-Bliesner, B. L., Tomas, R. A. & Gao, C. Role of eruption
316 season in reconciling model and proxy responses to tropical volcanism. *Proc. Natl. Acad.*

- 317 *Sci. U. S. A.* **114**, 1822–1826 (2017).
- 318 16. Toohey, M., Krüger, K., Sigl, M., Stordal, F. & Svensen, H. Climatic and societal impacts of
319 a volcanic double event at the dawn of the Middle Ages. *Clim. Change* **136**, 401–412
320 (2016).
- 321 17. Büntgen, U. *et al.* Cooling and societal change during the Late Antique Little Ice Age from
322 536 to around 660 AD. *Nat. Geosci.* **9**, 231–236 (2016).
- 323 18. Briffa, K. R., Jones, P. D., Schweingruber, F. H. & Osborn, T. J. Influence of volcanic
324 eruptions on Northern Hemisphere summer temperature over the past 600 years.
325 *Nature* **393**, 450–455 (1998).
- 326 19. Wilson, R. *et al.* Last millennium northern hemisphere summer temperatures from tree
327 rings: Part I: The long term context. *Quat. Sci. Rev.* **134**, 1–18 (2016).
- 328 20. Stoffel, M. *et al.* Estimates of volcanic-induced cooling in the Northern Hemisphere over
329 the past 1,500 years. *Nat. Geosci.* **8**, 784–788 (2015).
- 330 21. Schneider, L. *et al.* Revising midlatitude summer temperatures back to A.D. 600 based on
331 a wood density network. *Geophys. Res. Lett.* **42**, 4556–4562 (2015).
- 332 22. Toohey, M. & Sigl, M. Volcanic stratospheric sulfur injections and aerosol optical depth
333 from 500 BCE to 1900 CE. *Earth Syst. Sci. Data* **9**, 809–831 (2017).
- 334 23. Gao, C., Oman, L., Robock, A. & Stenchikov, G. L. Atmospheric volcanic loading derived
335 from bipolar ice cores: Accounting for the spatial distribution of volcanic deposition. *J.*
336 *Geophys. Res.* **112**, D09109 (2007).
- 337 24. Oman, L. *et al.* Modeling the distribution of the volcanic aerosol cloud from the 1783–
338 1784 Laki eruption. *J. Geophys. Res.* **111**, D12209 (2006).

- 339 25. Guo, S., Bluth, G. J. S., Rose, W. I., Watson, I. M. & Prata, A. J. Re-evaluation of SO₂
340 release of the 15 June 1991 Pinatubo eruption using ultraviolet and infrared satellite
341 sensors. *Geochemistry Geophys. Geosystems* **5**, Q04001 (2004).
- 342 26. Toohey, M., Krüger, K., Niemeier, U. & Timmreck, C. The influence of eruption season on
343 the global aerosol evolution and radiative impact of tropical volcanic eruptions. *Atmos.*
344 *Chem. Phys.* **11**, 12351–12367 (2011).
- 345 27. Kravitz, B. & Robock, A. Climate effects of high-latitude volcanic eruptions: Role of the
346 time of year. *J. Geophys. Res.* **116**, D01105 (2011).
- 347 28. Global Volcanism Program. Volcanoes of the World, v. 4.4.1. Venzke, E (ed.). Smithsonian
348 Institution. Downloaded 13 Oct 2015. <https://doi.org/10.5479/si.GVP.VOTW4-2013>
349 (2013).
- 350 29. D'Arrigo, R., Wilson, R. & Tudhope, A. The impact of volcanic forcing on tropical
351 temperatures during the past four centuries. *Nat. Geosci.* **2**, 51–56 (2008).
- 352 30. Plumb, R. A. Stratospheric Transport. *J. Meteorol. Soc. Japan* **80**, 793–809 (2002).
- 353 31. Holton, J. R. *et al.* Stratosphere-Troposphere Exchange. *Rev. Geophys.* **33**, 403–439
354 (1995).
- 355 32. Timmreck, C. *et al.* Aerosol size confines climate response to volcanic super-eruptions.
356 *Geophys. Res. Lett.* **37**, L24705 (2010).
- 357 33. Lacis, A. Volcanic aerosol radiative properties. *PAGES News!* **23**, 50–51 (2015).
- 358 34. Stenchikov, G. L. *et al.* Radiative forcing from the 1991 Mount Pinatubo volcanic
359 eruption. *J. Geophys. Res.* **103**, 13837–13857 (1998).
- 360 35. Forster, P. M. *et al.* Recommendations for diagnosing effective radiative forcing from

- 361 climate models for CMIP6. *J. Geophys. Res. Atmos.* **121**, 12,460–12,475 (2016).
- 362 36. Hansen, J. *et al.* Efficacy of climate forcings. *J. Geophys. Res.* **110**, D18104 (2005).
- 363 37. Shindell, D. & Faluvegi, G. Climate response to regional radiative forcing during the
364 twentieth century. *Nat. Geosci.* **2**, 294–300 (2009).
- 365 38. Shindell, D. T., Faluvegi, G., Rotstayn, L. & Milly, G. Spatial patterns of radiative forcing
366 and surface temperature response. *J. Geophys. Res. Atmos.* **120**, 5385–5403 (2015).
- 367 39. Glaze, L. S. & Baloga, S. M. Sensitivity of buoyant plume heights to ambient atmospheric
368 conditions: Implications for volcanic eruption columns. *J. Geophys. Res.* **101**, 1529–1540
369 (1996).
- 370 40. Sparks, R. S. J. The dimensions and dynamics of volcanic eruption columns. *Bull. Volcanol.*
371 **48**, 3–15 (1986).
- 372 41. Hildreth, W. & Fierstein, J. *The Novarupta-Katmai eruption of 1912--largest eruption of*
373 *the twentieth century: centennial perspectives*. U.S. Geological Survey Professional Paper
374 1791, 259 p., available at <https://pubs.usgs.gov/pp/1791/>, (2012).
- 375 42. Crowley, T. J. & Unterman, M. B. Technical details concerning development of a 1200 yr
376 proxy index for global volcanism. *Earth Syst. Sci. Data* **5**, 187–197 (2013).
- 377 43. Schmidt, G. A. *et al.* Climate forcing reconstructions for use in PMIP simulations of the
378 last millennium (v1.0). *Geosci. Model Dev.* **4**, 33–45 (2011).
- 379 44. Cole-Dai, J. *et al.* Cold decade (AD 1810–1819) caused by Tambora (1815) and another
380 (1809) stratospheric volcanic eruption. *Geophys. Res. Lett.* **36**, L22703 (2009).
- 381 45. Guillet, S. *et al.* Climate response to the Samalas volcanic eruption in 1257 revealed by
382 proxy records. *Nat. Geosci* **10**, 123–128 (2017).

- 383 46. Jensen, B. J. L. *et al.* Transatlantic distribution of the Alaskan White River Ash. *Geology*
384 **42**, 875–878 (2014).
- 385 47. Sun, C. *et al.* Ash from Changbaishan Millennium eruption recorded in Greenland ice:
386 Implications for determining the eruption’s timing and impact. *Geophys. Res. Lett.* **41**,
387 694–701 (2014).
- 388 48. Oppenheimer, C. *et al.* The Eldgjá eruption: timing, long-range impacts and influence on
389 the Christianisation of Iceland. *Clim. Change* **147**, 369–381 (2018).
- 390 49. Baroni, M., Savarino, J., Cole-Dai, J., Rai, V. K. & Thiemens, M. H. Anomalous sulfur
391 isotope compositions of volcanic sulfate over the last millennium in Antarctic ice cores. *J.*
392 *Geophys. Res.* **113**, D20112 (2008).
- 393 50. Savarino, J., Romero, A., Cole-Dai, J., Bekki, S. & Thiemens, M. H. UV induced mass-
394 independent sulfur isotope fractionation in stratospheric volcanic sulfate. *Geophys. Res.*
395 *Lett.* **30**, 2131 (2003).
- 396 51. Lanciki, A., Cole-Dai, J., Thiemens, M. H. & Savarino, J. Sulfur isotope evidence of little or
397 no stratospheric impact by the 1783 Laki volcanic eruption. *Geophys. Res. Lett.* **39**,
398 L01806 (2012).
- 399 52. Thordarson, T. & Larsen, G. Volcanism in Iceland in historical time: Volcano types,
400 eruption styles and eruptive history. *J. Geodyn.* **43**, 118–152 (2007).
- 401 53. Oppenheimer, C. *et al.* Multi-proxy dating the ‘Millennium Eruption’ of Changbaishan to
402 late 946 CE. *Quat. Sci. Rev.* **158**, 164–171 (2017).
- 403 54. Stothers, R. B. Mystery cloud of AD 536. *Nature* **307**, 344–345 (1984).
- 404 55. Watt, S. F. L., Pyle, D. M. & Mather, T. A. The volcanic response to deglaciation: Evidence

405 from glaciated arcs and a reassessment of global eruption records. *Earth-Science Rev.*
406 **122**, 77–102 (2013).

407 **Acknowledgements**

408 This work was supported by the Federal Ministry for Education and Research in Germany
409 (BMBF) through the research program “MiKlip” (FKZ:01LP130B, 01LP1130A and 01LP1517B).
410 MT additionally acknowledges support by the Deutsche Forschungsgemeinschaft (DFG) in the
411 framework of the priority programme “Antarctic Research with comparative investigations in
412 Arctic ice areas” through grant TO 967/1-1. KK and M. Sigl acknowledge support through the
413 NFR project “VIKINGS” (Project No. 275191). CT additionally acknowledges support from
414 supported by the European Union project StratoClim (FP7-ENV.2013.6.1-2). Computations were
415 performed at the German Climate Computer Center (DKRZ). The authors thank Lea Schneider
416 and coworkers for making their NH temperature reconstruction publically available. This paper
417 is a product of the Volcanic Impacts on Climate and Society (VICS) working group, as part of the
418 Past Global Changes (PAGES) project, which in turn received support from the US National
419 Science Foundation and the Swiss Academy of Sciences.

420 **Author Contributions**

421 M.T., K.K., C.T. and H.S. designed the model experiments. M.T. performed the model
422 simulations and analysis with input from K.K., C.T., and H.S. M.T. performed the analysis of tree-
423 ring temperature reconstructions and volcanic stratospheric sulfur injections with input from
424 M. Sigl, M. Stoffel and R.W. M.T. led the manuscript writing with input from all coauthors.

425 **Competing Financial Interests statement**

426 The authors declare no competing financial interests.

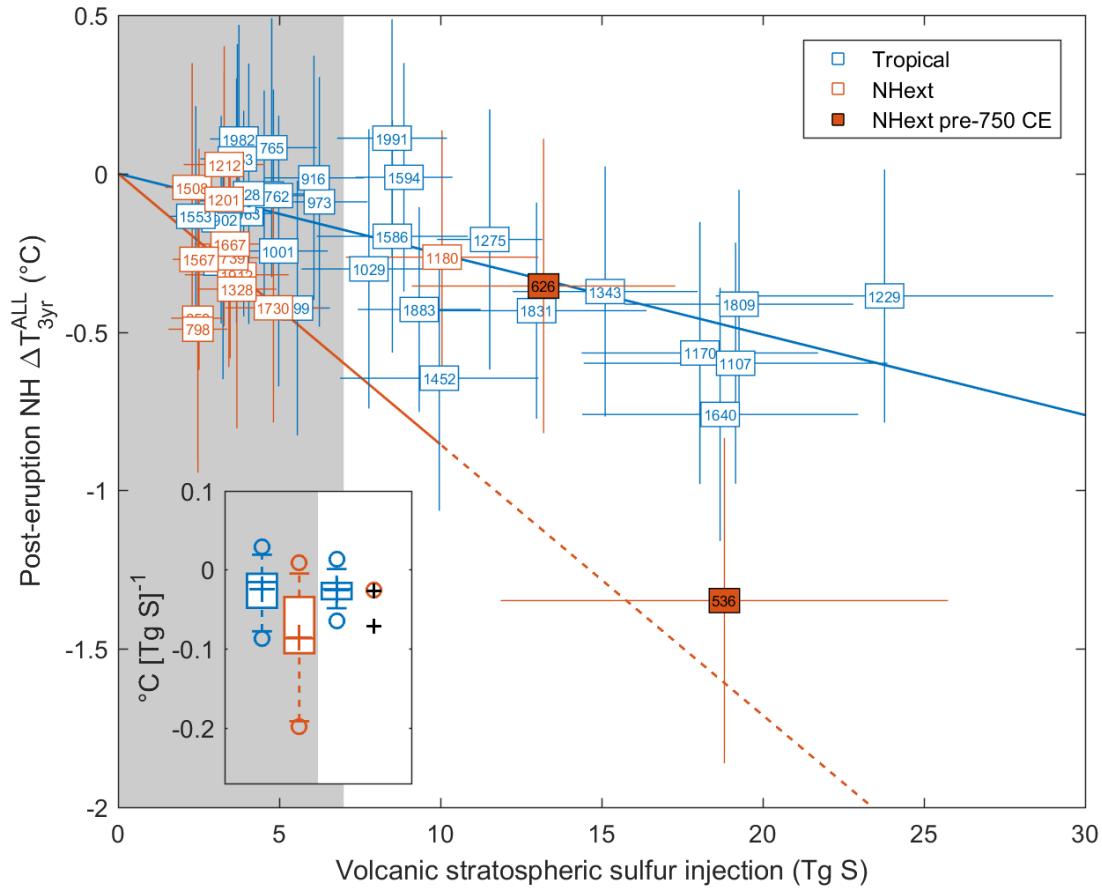
427 **Tables**

428 **Table 1: Ratios of hemispheric temperature anomalies to stratospheric sulfur injection (VSSI)**
 429 **ratios for tropical and NH extratropical explosive eruptions.** Mean $\Delta T/VSSI$ values over the
 430 tropical (“trop”) and extratropical (“extrop”) events listed in Supplementary Tables 4 and 5,
 431 with 1σ standard error of the mean are listed for the N-TREND¹⁹, STO15²⁰, SCH15²¹ and NH
 432 temperature reconstructions, along with that from the composite mean of the three
 433 reconstructions (ALL). Percent differences between mean extratropical and tropical $\Delta T/VSSI$
 434 values are listed with 1σ uncertainties. Percent differences between mean extratropical and
 435 tropical $\Delta T/VSSI$ values are repeated in the final row with VSSI for extratropical eruptions
 436 adjusted ($VSSI^* = VSSI/0.57$) such that the scaling from ice core sulfate flux to VSSI is the
 437 same for both tropical and extratropical eruptions.

	N-TREND	STO15	SCH15	ALL
$\frac{\Delta T}{VSSI} _{\text{trop}}$ ($^{\circ}\text{C} [\text{Tg S}]^{-1}$)	-0.019 ± 0.006	-0.036 ± 0.009	-0.021 ± 0.003	-0.025 ± 0.005
$\frac{\Delta T}{VSSI} _{\text{extrop}}$ ($^{\circ}\text{C} [\text{Tg S}]^{-1}$)	-0.081 ± 0.020	-0.102 ± 0.024	-0.059 ± 0.018	-0.080 ± 0.018
$\frac{\Delta T}{VSSI} _{\text{extrop}} - \frac{\Delta T}{VSSI} _{\text{trop}}$ (%)	330 ± 150	180 ± 82	180 ± 94	220 ± 85
$\frac{\Delta T}{VSSI^*} _{\text{extrop}} - \frac{\Delta T}{VSSI} _{\text{trop}}$ (%)	150 ± 87	58 ± 47	61 ± 54	81 ± 48

438

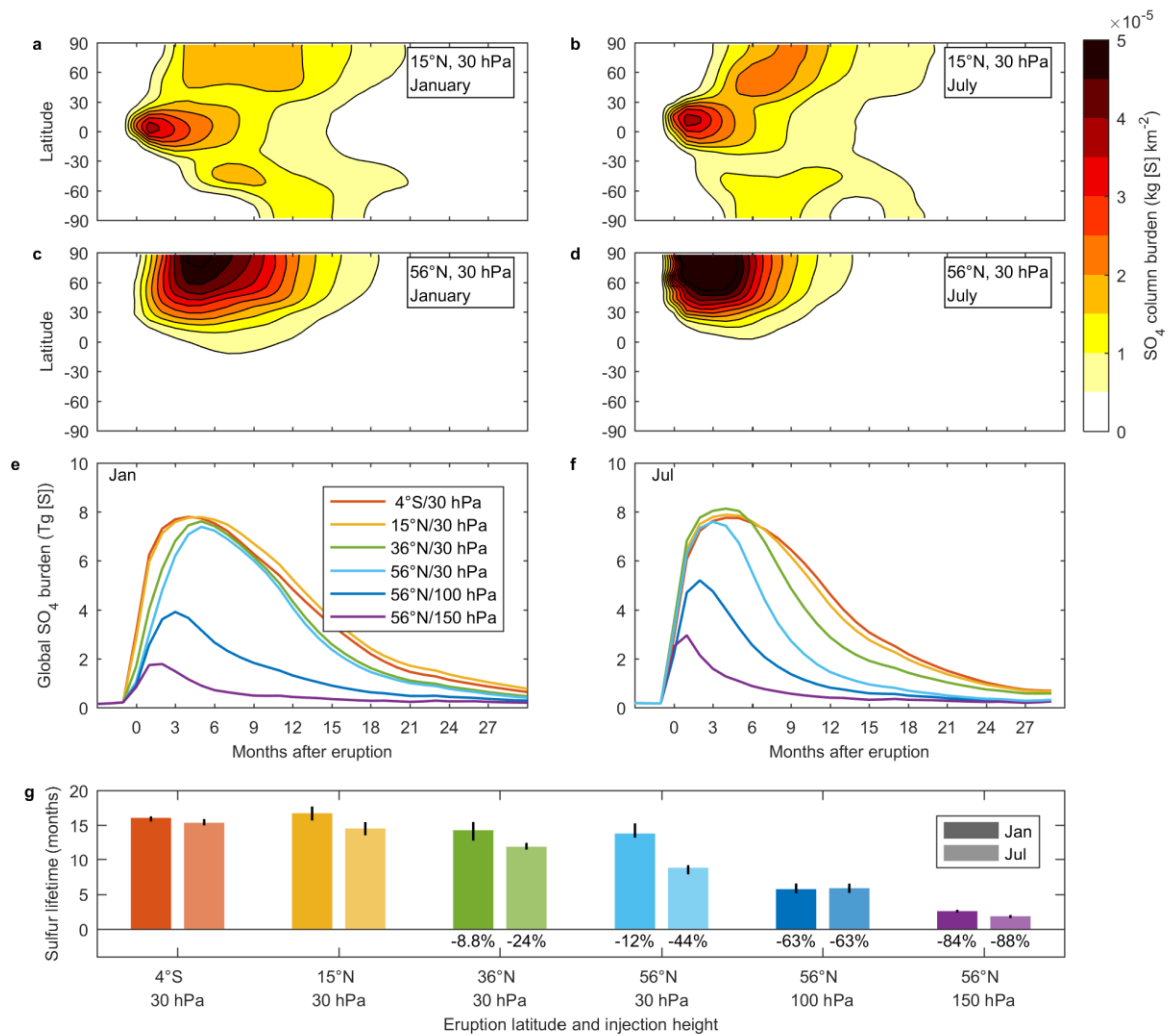
439 **Figures**



440
 441 **Figure 1: Reconstructed post-volcanic NH temperature response to NH extratropical and**
 442 **tropical eruptions in relation to volcanic stratospheric sulfur injection.** Three-year mean
 443 temperature anomalies (ΔT_{3yr}^{ALL}) are plotted versus estimated volcanic stratospheric sulfur
 444 injection (VSSI, Tg [S]) for (blue) tropical and (orange) extratropical explosive eruptions. Number
 445 labels indicate eruption years. Vertical and horizontal error bars represent $\pm 1\sigma$ uncertainties.
 446 The 1257 Samalas eruption (see Supplementary Table 4), lies outside the chosen limits of the
 447 plot. Colored lines indicate the mean ΔT -to-VSSI ratio for both tropical and extratropical
 448 eruptions after 750 CE. Temperature anomalies for NH extratropical events before 750 CE are
 449 shown with orange-filled markers. **Inset panel** shows boxplots of the distribution of three-year

450 mean NH temperature anomalies per unit VSSI. Boxplots are shown separately for eruptions
451 with VSSI less than (gray shading on both plots) and greater than 7 Tg S. Crosses denote the
452 distribution mean, horizontal line the median, box the 25-75% interquantile range, whiskers the
453 1-99% interquantile range, and outliers are marked with circles. For extratropical eruptions with
454 VSSI>7 Tg S, markers show cooling-to-VSSI ratios for individual eruptions in orange (post-750
455 CE) and black (pre-750 CE).

456

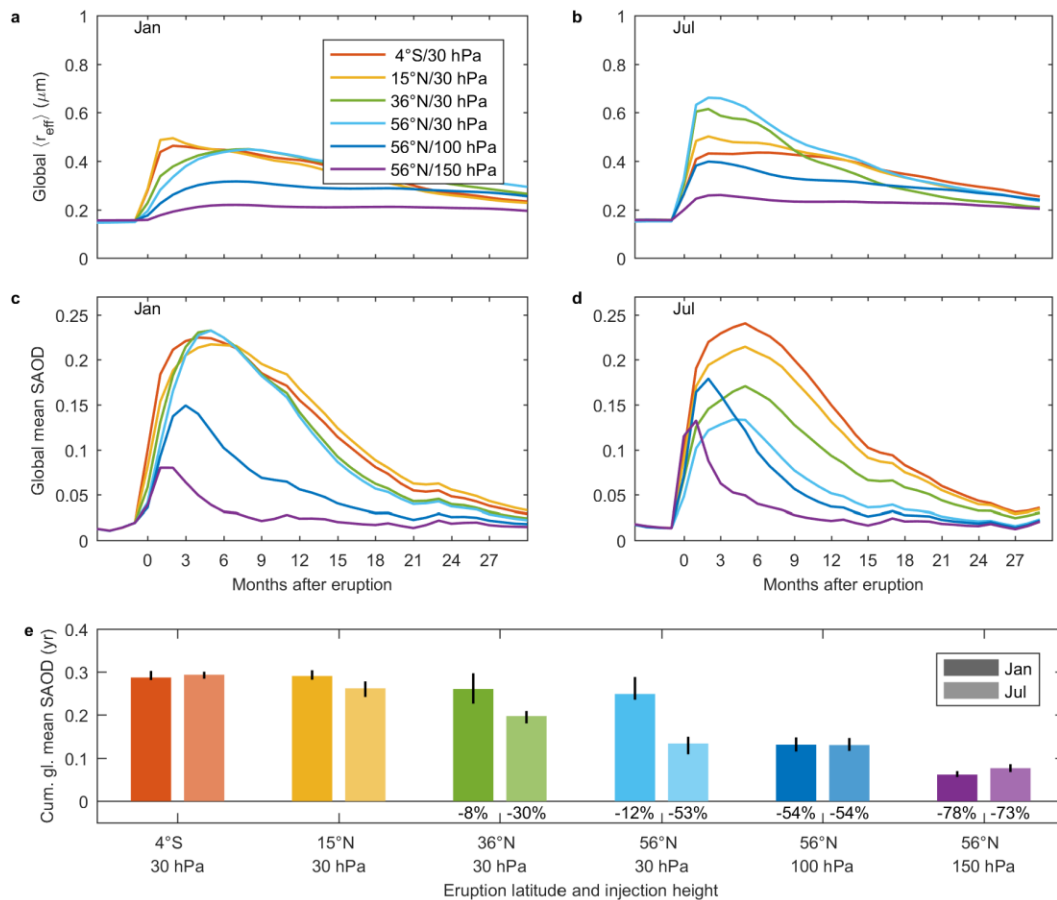


457
 458 **Figure 2: Simulated volcanic stratospheric aerosol burdens and lifetimes for varying eruption**
 459 **latitude, season and injection height.** Ensemble mean zonal mean aerosol burdens (in kg [S]
 460 km⁻²) are shown for (a, b) tropical (15°N) and (c, d) extratropical (56°N) eruptions of 8.5 Tg S in
 461 (a, c) January and (b, d) July. Ensemble mean global sulfur burden (Tg [S]) time series are shown
 462 (e, f) for the six simulated injection locations. Line colors denote injection latitude and heights
 463 as listed in legend of panel (e). In panel (g) stratospheric sulfur e-folding lifetimes are shown for
 464 each eruption latitude and injection height, with black whiskers indicating the full ensemble
 465 spread. For the extratropical injection cases, text labels show the percent difference of sulfur e-

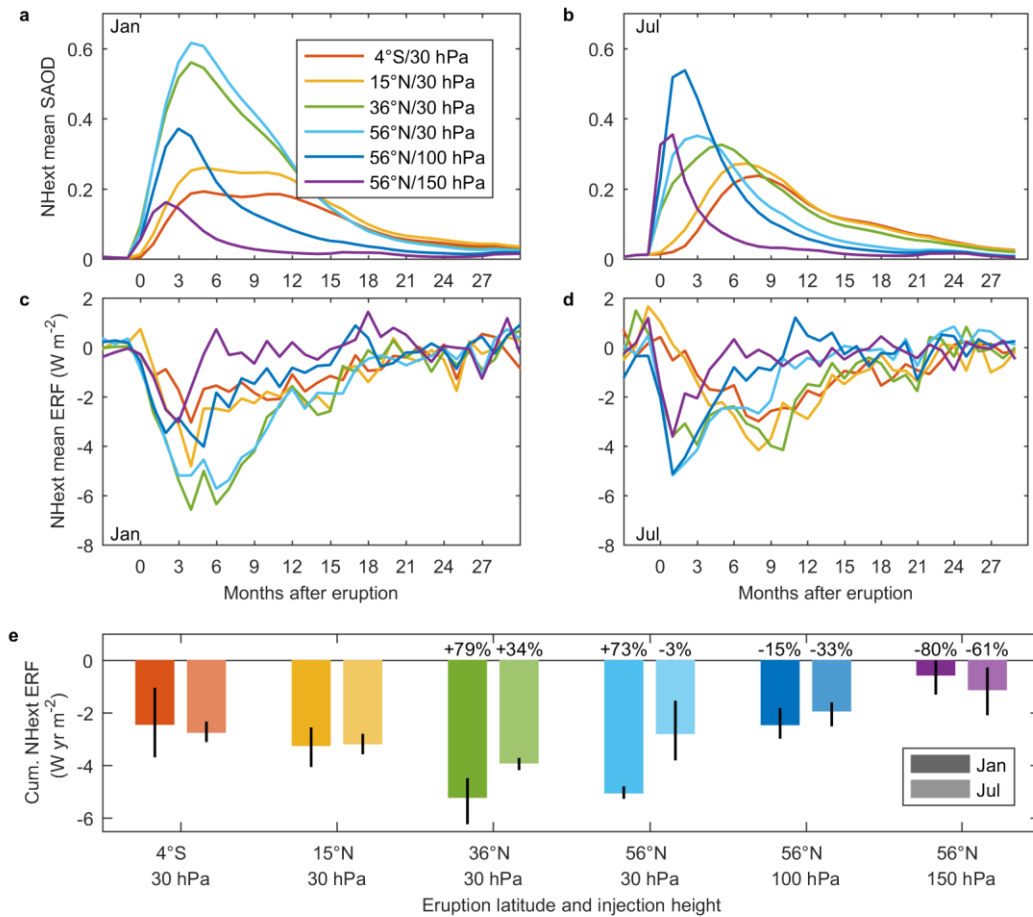
466 folding lifetime with respect to the mean of the tropical (4°S and 15°N, 30 hPa) injection

467 eruption simulations.

468



469
 470 **Figure 3: Simulated global mean volcanic aerosol properties for varying eruption latitude,**
 471 **season and injection height.** Panels show (a, b) ensemble mean sulfate-weighted effective
 472 radius ($\langle r_{\text{eff}} \rangle$), and (c,d) ensemble mean stratospheric aerosol optical depth (SAOD), from
 473 simulated eruptions of 8.5 Tg S in (left) January and (right) July. Line colors denote injection
 474 latitude and heights as listed in legend of panel (c). Three-year cumulative SAOD is shown in
 475 panel (e) as a function of injection latitude and height, with black whiskers indicating the full
 476 ensemble spread. For the extratropical injection cases, text labels show the percent difference
 477 of cumulative SAOD with respect to the mean of the tropical (4°S and 15°N, 30 hPa) injection
 478 eruption simulations.



479
 480 **Figure 4: Simulated volcanic SAOD and effective radiative forcing over the NH extratropics**
 481 **(30-90°N) for varying eruption latitude, season and injection height.** Shown are (a,b) SAOD
 482 and (d,e) effective radiative forcing (ERF) for simulated eruptions of 8.5 Tg S in (left) January
 483 and (right) July. Line colors denote injection latitude and heights as listed in legend of panel (a).
 484 Three-year cumulative NHext ERF is shown in panel (e) as a function of injection latitude and
 485 height, with black lines indicating the full ensemble spread. For the extratropical injection
 486 cases, text labels show the percent difference of cumulative ERF with respect to the mean of
 487 the tropical (4°S and 15°N, 30 hPa) injection eruption simulations.

488

489 **Methods**

490 **Volcanic stratospheric sulfur injections**

491 Volcanic stratospheric sulfur injection (VSSI) estimates before 1900 CE are taken from the
492 eVolv2k database²², based on analysis of bipolar ice core arrays. For the 20th Century, satellite
493 observations⁷ are used for estimates of VSSI for Pinatubo (1991) and El Chichón (1982). For
494 eruptions between 1900 and the start of the satellite era, we used Antarctic and Greenland ice
495 core sulfate fluxes from the ICI reconstruction of Ref 42, and applied the scaling methodology
496 used in the construction of eVolv2k. Categorization of eruptions as tropical or extratropical is
497 provided by the eVolv2k reconstruction based on the presence or lack of bipolar ice core sulfate
498 signals, or from observations for 20th Century eruptions. Eruption years for unidentified tropical
499 eruptions are adjusted one year earlier than listed in the eVolv2k database, to account for the
500 typical 1-year lag between eruption and ice sheet deposition. All unidentified eruptions are
501 thereafter assumed to have a dating uncertainty of ± 1 year for 1750-1900 CE and ± 2 years from
502 500-1750 CE.

503 **Post eruption Northern Hemisphere temperature anomalies**

504 Based on the compiled VSSI record, we first select tropical and NH extratropical volcanic events
505 between 500-2000 CE with estimated VSSI greater than 2 Tg S. From this list, in order to
506 exclude events in which cooling from the eruption in question may be superimposed on the
507 return to normal conditions after a preceding eruption, we exclude events for which an
508 eruption of magnitude greater than 2 Tg S occurred within the preceding 6 years, and also
509 those for which an event greater than 10 Tg S occurred within the preceding 10 years. This
510 process excluded 17 eruptions (Supplementary Table 1), including well known examples such as

511 Tambora (1815) and an unidentified eruption of ca. 1457 CE. Extratropical eruptions which are
 512 known or suspected to have been characterized by some degree of effusive eruption style,
 513 including the strong Icelandic “fire” eruptions of Laki (1783-84) and Eldgjá (939) have also been
 514 excluded (Supplementary Table 2): the remaining extratropical events are assumed to
 515 represent extratropical explosive events although it should be clear that this list likely includes
 516 signals from additional Icelandic effusive events.

517 For each volcanic event, NH summer temperature anomalies are constructed using three recent
 518 reconstructions^{19–21}. First, based on a simple mean of the three reconstructions, eruption dates
 519 for unidentified eruptions are adjusted within the dating uncertainty to maximize the post-
 520 eruption 3 year mean cooling anomaly. This adjustment aims to take into account uncertainty
 521 in the dating of the ice core signals, but also the possible shift related to eruptions occurring
 522 before or after summer of any calendar year. Temperature anomalies for each event and each
 523 temperature reconstruction are then calculated with respect to the preceding 5 years. Given an
 524 estimated eruption at year y_0 , NH 3 year mean temperature anomalies (ΔT_{3yr}) are calculated as
 525 follows for tropical and NH extratropical eruptions:

	Tropical eruption	NH extratropical eruption
ΔT_{3yr} : Three year mean anomaly	$\frac{1}{3} \sum_{i=1}^3 T_{y_0+i} - \frac{1}{5} \sum_{i=-5}^{-1} T_{y_0+i}$	$\frac{1}{3} \sum_{i=0}^2 T_{y_0+i} - \frac{1}{5} \sum_{i=-5}^{-1} T_{y_0+i}$

526
 527 Uncertainties (σ) in the tree ring-based temperature reconstructions are taken from the
 528 original data sets. Uncertainties in post volcanic three year temperature anomalies and multi-

529 reconstruction means are calculated using reported uncertainties and standard rules of error
530 propagation.

531 **MAECHAM5-HAM**

532 Simulations of volcanic stratospheric sulfur injections are performed with the aerosol-climate
533 model MAECHAM5-HAM^{26,56,57}. The spatial resolution is ~2.8° by 2.8°, with T42 spectral
534 truncation and 39 vertical levels up to 0.01 hPa (~80 km). The atmospheric component of the
535 model is free running, while sea surface temperatures are prescribed as an annually repeating
536 climatology.

537 Volcanic simulations are initiated by the injection of SO₂ into a specified model grid box and
538 height. A sulfur chemistry module converts SO₂ to H₂SO₄ via the reactions:



539 The rate of SO₂ to H₂SO₄ conversion depends on concentrations of hydroxyl radical (OH) taken
540 from prior chemistry–climate model simulations⁵⁸. The use of prescribed OH concentrations
541 neglects potential changes in H₂SO₄ production rates due to local consumption of OH, which is
542 thought to play an important role for extremely large eruptions⁵⁹. The prescribed monthly
543 mean OH fields contain significant spatial structure (Supplementary Fig. 5), with very low
544 concentrations in polar winter due to the dependence of OH production on solar insolation.
545 There is also a strong vertical gradient in OH concentrations through the lower and middle

546 stratosphere, due to changes in solar ultraviolet radiative flux and the availability of H₂O, which
547 has a minimum around the level of the tropopause.

548 After oxidation of the volcanic SO₂ source gas, H₂SO₄ condenses with water to form sulfate
549 (SO₄) aerosol. Aerosol processes in MAECHAM5-HAM are calculated by the aerosol
550 microphysical module HAM⁶⁰, and include aerosol formation and growth via nucleation,
551 condensation, accumulation, and coagulation; vertical redistribution via sedimentation; and
552 finally the removal processes wet and dry deposition.

553 Pinatubo-magnitude simulations with MAECHAM5-HAM have resulted in good agreement with
554 observations in terms of the aerosol optical depth (AOD), top of atmosphere short-wave
555 radiation anomalies, and aerosol effective radius^{26,56}. The MAECHAM5-HAM configuration used
556 here has no quasi-biennial oscillation (QBO): winds in the equatorial stratosphere are easterly
557 throughout the year, and therefore variability of stratospheric dynamics⁶¹ and aerosol transport
558 related to the QBO are not included in the simulations. The decay of simulated AOD was found
559 to be slightly faster than that observed, which is perhaps related to a slight high-bias in the
560 simulated aerosol effective radius⁵⁶. On the other hand, consistency in the timing of
561 extratropical AOD peak values suggests the model reproduces well the seasonal variation in
562 aerosol transport²⁶. For tropical eruptions of Pinatubo magnitude and below, the model
563 produces a linear relationship between radiative forcing and VSSI⁶².

564 **Model experiments**

565 To isolate the impact of eruption latitude on the aerosol evolution and resulting radiative
566 forcing, we performed ensemble MAECHAM5-HAM simulations with a fixed magnitude of

567 volcanic stratospheric sulfur injection at various latitudes, months and injection heights. We
568 choose the estimated VSSI of the 1991 eruption of Pinatubo (17 Tg SO₂ or equivalently 8.5 Tg [S]
569 injection), since observations of the Pinatubo aerosol provide the best estimates of sulfur
570 injection, aerosol evolution and radiative forcing of any major volcanic eruption, making it a
571 standard modeling validation experiment. Simulation eruption locations are chosen based on
572 the global distribution of identified volcanic eruptions with Volcanic Explosivity Index equal to
573 or greater than 5 (Supplementary Fig. 2) according to the Volcanoes of the World (VOTW)
574 database²⁸. Four 10-degree latitude ranges contain 57% of all VEI ≥ 5 eruptions in the VOTW
575 database: in order of eruption frequency, these latitude bands are 50-60°N, 30-40°N, 0-10°S,
576 and 10-20°N. For each of these four latitude ranges, we chose a “typical” eruption location,
577 roughly consistent with the highest density of identified eruptions, sampling global eruptions
578 hot spots including Indonesia, Central America, Japan and Alaska (Supplementary Table 6). The
579 chosen eruption locations are spread evenly between the western and eastern coasts of the
580 Pacific Ocean, although model simulations suggest no significant impact of the eruption
581 longitude on the aerosol evolution following explosive tropical eruptions²⁶. To include the
582 potential impacts of eruption season, simulations are performed with eruptions in both January
583 and July. This choice of months is somewhat arbitrary, but is motivated by: (1) the common use
584 of January 1 as a standard eruption date for eruptions on unknown eruption timing in volcanic
585 forcing reconstructions^{22,42}; (2) the rough agreement of July 1 with the actual seasonal timing of
586 the Pinatubo eruption (on June 15, 1991); and (3) the fact that NH radiative anomalies from
587 January and July tropical eruptions nearly span the full range of SAOD and radiative forcing seen
588 in model simulations using a fuller sample of eruption season distribution²⁶. Since the spatial

589 spread of aerosol is sensitive to the meteorological conditions at the time of the eruption⁶³,
590 ensembles of simulation were performed. For each of the four eruption locations, we
591 performed ten MAECHAM-HAM eruption simulations with SO₂ injection at 30 hPa (~23 km), five
592 simulations each for injections in January and July. To investigate the impact of injection height
593 for extratropical eruptions, simulations at 56°N were repeated with injection heights of 100 hPa
594 (~16 km) and 150 hPa (~13 km), with again, five simulations for January eruptions, and five
595 simulations for July eruptions.

596 A 30 year control run was performed with no stratospheric sulfur injections, with all other
597 boundary conditions and forcings identical to the eruptions simulations.

598 **Model output**

599 Sulfate aerosol column burdens and stratospheric aerosol optical depth (SAOD) are output
600 directly by the model, and zonal means over the full globe and the NH extratropics were
601 calculated using area-weighted means. Stratospheric sulfur lifetimes are calculated as the time
602 taken for the total sulfur (SO₂ + H₂SO₄) to cross 1/*e* of the injected amount—this metric is
603 typically longer than lifetimes calculated based on the decay of sulfate after its peak value, but
604 is a better measure of the efficiency of loss processes since the timing of the sulfate peak also
605 depends on the rate of SO₂-to-H₂SO₄ conversion. Sulfate aerosol effective radius (r_{eff}), a
606 function of height, latitude and longitude, was averaged in space using sulfate aerosol mass as a
607 weighting function. The resulting sulfate-mass-weighted, $\langle r_{\text{eff}} \rangle$, represents the typical r_{eff} in the
608 region of the most sulfate aerosol, which will dominate the radiative transfer calculations. Net
609 (shortwave + longwave) top of atmosphere (TAO) radiative anomalies were calculated as the

610 difference radiative fluxes between each eruption simulation and the control run climatology,
611 corresponding to the “fixed SST” effective radiative forcing (ERF) quantity^{35,36}.

612 **Data availability**

613 Volcanic stratospheric sulfur injection estimates used in this study are available in the World
614 Data Center for Climate hosted by the German Climate Computing Center (DKRZ) with the
615 identifier doi:10.1594/WDCC/eVolv2k_v1. NH temperature reconstructions used are available
616 from the NOAA/World Data Service for Paleoclimatology archives via links
617 <https://www.ncdc.noaa.gov/paleo-search/study/19743>, [https://www.ncdc.noaa.gov/paleo-](https://www.ncdc.noaa.gov/paleo-search/study/19039)
618 [search/study/19039](https://www.ncdc.noaa.gov/paleo-search/study/19039), and <https://www.ncdc.noaa.gov/paleo-search/study/18875>.

619 **Code availability**

620 The Matlab scripts used for the analyses described in this study can be obtained from the
621 corresponding author upon reasonable request.

622 **References**

- 623 56. Niemeier, U. *et al.* Initial fate of fine ash and sulfur from large volcanic eruptions. *Atmos.*
624 *Chem. Phys.* **9**, 9043–9057 (2009).
- 625 57. Toohey, M., Krüger, K. & Timmreck, C. Volcanic sulfate deposition to Greenland and
626 Antarctica: A modeling sensitivity study. *J. Geophys. Res. Atmos.* **118**, 4788–4800 (2013).
- 627 58. Timmreck, C., Graf, H.-F. & Steil, B. in *Volcanism and the Earth’s Atmosphere* (eds.
628 Robock, A. & Oppenheimer, C.) **139**, 213–225 (American Geophysical Union, 2003).
- 629 59. Bekki, S. Oxidation of volcanic SO₂: A sink for stratospheric OH and H₂O. *Geophys. Res.*
630 *Lett.* **22**, 913–916 (1995).

- 631 60. Stier, P. *et al.* The aerosol-climate model ECHAM5-HAM. *Atmos. Chem. Phys.* **5**, 1125–
632 1156 (2005).
- 633 61. Punge, H. J., Konopka, P., Giorgetta, M. A. & Müller, R. Effects of the quasi-biennial
634 oscillation on low-latitude transport in the stratosphere derived from trajectory
635 calculations. *J. Geophys. Res.* **114**, D03102 (2009).
- 636 62. Metzner, D. *et al.* Radiative forcing and climate impact resulting from SO₂ injections
637 based on a 200,000-year record of Plinian eruptions along the Central American Volcanic
638 Arc. *Int. J. Earth Sci.* **103**, 2063–2079 (2014).
- 639 63. Jones, A. C., Haywood, J. M., Jones, A. & Aquila, V. Sensitivity of volcanic aerosol
640 dispersion to meteorological conditions: A Pinatubo case study. *J. Geophys. Res. Atmos.*
641 **121**, 6892–6908 (2016).